Earth and Planetary Science Letters 607 (2023) 118075

Contents lists available at ScienceDirect

Earth and Planetary Science Letters

journal homepage: www.elsevier.com/locate/epsl

Climax in Wrangellia LIP activity coincident with major Middle Carnian (Late Triassic) climate and biotic changes: Mercury isotope evidence from the Panthalassa pelagic domain

Xin Jin [a,*], Yuki Tomimatsu [b,c], Runsheng Yin [d,*], Tetsuji Onoue [c], Marco Franceschi [e], Stephen E. Grasby [f], Yixing Du [a], Manuel Rigo [g]

[a] State Key Laboratory of Oil and Gas Reservoir Geology and Exploitation and Key Laboratory of Deep-time Geography and Environment Reconstruction and Applications of Ministry of Natural Resources, Chengdu University of Technology, Chengdu 610059, China
[b] Department of Earth and Environmental Sciences, Kumamoto University, Kumamoto 860-8555, Japan
[c] Department of Earth and Planetary Sciences, Kyushu University, Fukuoka 812-8581, Japan
[d] State Key Laboratory of Ore Deposit Geochemistry, Institute of Geochemistry, Chinese Academy of Sciences, Guiyang, 550081, China
[e] Department of Mathematics and Geosciences, University of Trieste, via Weiss, 2, 34128 Trieste, Italy
[f] Geological Survey of Canada, Natural Resources Canada, 3303 33rd Street N.W., Calgary, Alberta T2L 2A7, Canada
[g] Dipartimento di Geoscienze, Università degli Studi di Padova, Via G. Gradenigo 6, Padova, Italy

ARTICLE INFO

Article history:
Received 1 December 2022
Received in revised form 16 February 2023
Accepted 18 February 2023
Available online 2 March 2023
Editor: A. Jacobson

Keywords:
Carnian Pluvial Episode
mercury mass-independent fractionation
volcanism
central Japan

ABSTRACT

The Carnian Pluvial Episode (CPE, ~233 Ma) was characterized by multiple negative carbon-isotope excursions, turnovers in marine and terrestrial biota, and a Tethys-wide humid climate accompanied by abundant terrigenous sediment and freshwater input into sedimentary basins. A general temporal coincidence between the CPE and the emplacement of the Wrangellia Large Igneous Province (Wrangellia LIP) has been well documented, however, it remains unclear whether fluctuations in the intensity of the LIP's activity could be linked to the biotic and climate changes at the CPE. We here present mercury (Hg) concentration and isotope ratio records from a pelagic deep-water succession (Section N-O, Inuyama, Japan) that encompasses the CPE interval. Data reveal concurrent peaks in the Hg concentrations and ratios of Hg to TOC and enrichment factors Th_{EF}, Al_{EF}, Zn_{EF}, and Ni_{EF} implying that excess Hg loading in the sediments occurred, likely due to volcanic activity, prior to the CPE siliciclastic input. Furthermore, Δ^{199}Hg values show a negative shift across the boundary between the Julian 1 and Julian 2, followed by a positive shift up to near-zero values at the Julian/Tuvalian transition. The near-zero Δ^{199}Hg values at the Julian/Tuvalian boundary are associated with an increase in Hg and Cu loading, suggesting a peak of volcanogenic Hg and Cu input that may indicate a climax in the Wrangellia LIP activity. Most notably, the Julian/Tuvalian transition is where evidence of the most pronounced changes in carbonate platform evolution, biological turnover and climate change associated with the event has been highlighted. Our results therefore suggest that variations in the intensity of LIP volcanism may have played a major role in driving biotic and climate changes during the CPE. Our results provide a model for other mass extinction events associated with LIPs (e.g., the end-Permian) where low-intensity background volcanism was punctuated by high-intensity pulses, these latter being the real killers.

1. Introduction

The Carnian Pluvial Episode (CPE, ~233 Ma) is a phase of climate and biotic changes that occurred in the Late Triassic (Simms and Ruffell, 1989). The CPE was first recognized from the global evidence of modifications in carbonate platform environments and increased terrigenous input into sedimentary basins, which started at the boundary between the Julian 1 and 2, and spanned the Julian 2 and Tuvalian 1, substages of the Carnian period (Simms and Ruffell, 1989; Breda et al., 2009; Dal Corso et al., 2018). It has been shown that the CPE is associated with multiple, globally recognized negative carbon-isotope excursions (NICEs) in terrestrial and marine δ^{13}C records. At least four NCIEs (NCIE 1 to NCIE 4; Fig. 1A) have been recognized and are thought to be evidence of multi-phase perturbation of the carbon cycle linked to multiple

* Corresponding authors.
E-mail addresses: jinxin19@cdut.edu.cn (X. Jin), yinrunsheng@mail.gyig.ac.cn (R. Yin).

https://doi.org/10.1016/j.epsl.2023.118075

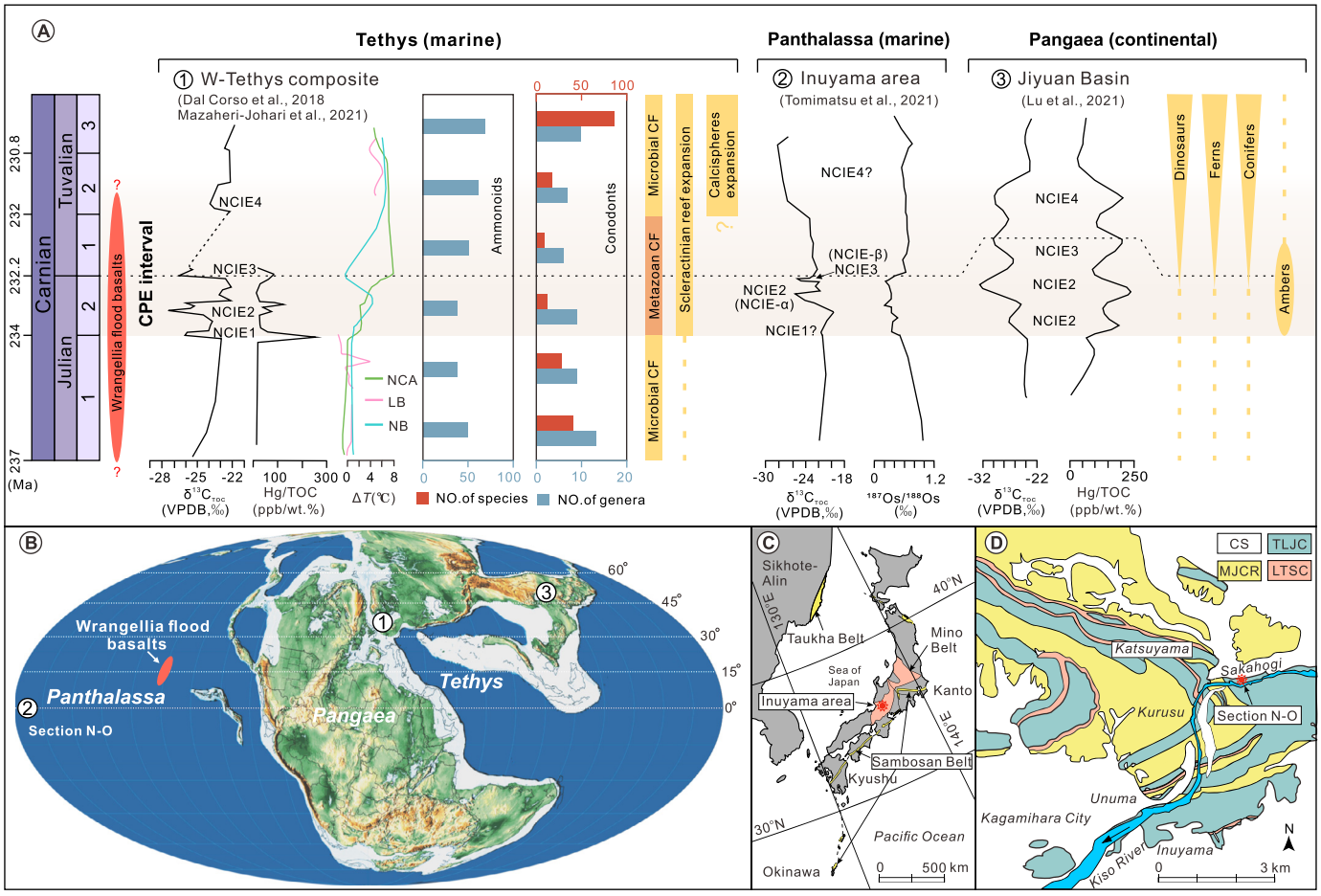

Fig. 1. A) Geochemical and biotic changes at the CPE in Tethys (marine), Panthalassa (marine) and Pangaea (continental). The duration of Wrangellia Large Igneous Province volcanism follows Greene et al. (2010) and Parrish and McNicoll (1992). The changes in marine and terrestrial biota, as well as the carbonate factory, follow Dal Corso et al. (2020). The sea-surface temperature curves are from Lagonegro Basin (LB, Rigo and Joachimski, 2010; Rigo et al., 2012; Trotter et al., 2015), Northern Calcareous Alps (NCA, Hornung et al., 2007) and Nanpanjiang Basin (NB, Sun et al., 2016). Temperature trends redrawn from Dal Corso et al. (2020). Note: Ferns refer to Matoniaceae and Dipteridaceae; Conifers refer to modern families, i.e., Podocarpaceae, Araucariaceae, Pinaceae (Dal Corso et al., 2020; Roghi et al., 2022). Microbial CF = Microbial carbonate factory; Metazoan CF = Metazoan carbonate factory. Carnian time scale follows Bernardi et al. (2018). B) Paleogeographic map of Carnian (Late Triassic) (Scotese, 2014) with the relative positions of Wrangellia LIP (e.g. Dal Corso et al., 2020), Alpine region (1 in A), Section N-O (2 in A) and Jiyuan Basin (3 in A). C) Positions of Mino and Sambosan belts in Japan. D) Geological map of the Inuyama area with the position of Section N-O (red marker). C-D are from Tomimatsu et al. (2021). CS = Cenozoic sediments; TLJC = Triassic to Lower Jurassic cherts; MJCR = Middle Jurassic clastic rocks; LTSC = Lower Triassic siliceous claystones.

pulses of volcanic activity of the Wrangellia Large Igneous Province (Wrangellia LIP; Fig. 1A; e.g., Dal Corso et al., 2018; Lu et al., 2021). Evidence from palynological assemblages, chemical weathering indices, $\delta^{18}O$ records from conodont apatite, and redox-sensitive elements suggest that the CPE was characterized by an extremely humid climate (e.g., Roghi, 2004; Baranyi et al., 2019), warm temperatures (Rigo and Joachimski, 2010; Rigo et al., 2012; Trotter et al., 2015; Sun et al., 2016) and marine anoxia (Soua, 2014; Sun et al., 2016; Tomimatsu et al., 2021). Shallow water carbonate production experienced synchronous modifications, in response to the climate changes and eustatic sea-level fall associated with this event (Jin et al., 2020, 2022a). The important climate and environmental changes at the CPE also impacted the biosphere, as testified by high extinction rates in ammonoids and conodonts (e.g., Rigo et al., 2007; Dal Corso et al., 2020), and significant radiation and diversification during or after the CPE in some important groups such as dinosaurs (Bernardi et al., 2018), scleractinian corals (Stanley, 2003), calcareous nannofossils and plants (e.g., Dal Corso et al., 2020; Fig. 1A).

A documented temporal coincidence between the Wrangellia LIP and the CPE (e.g., Furin et al., 2006; Dal Corso et al., 2020) has made volcanism one of the main candidates as the driver of the CPE. Although the cause-effect relationships between the observed changes in the Earth ecosystem and volcanism are subject of ongoing debate. The volcanism hypothesis is supported by the identification of multiple mercury (Hg) enrichments and increased input of unradiogenic osmium (Os) in sedimentary successions encompassing the CPE (Fig. 1A; Lu et al., 2021; Mazaheri-Johari et al., 2021; Tomimatsu et al., 2021; Zhao et al., 2022).

Mercury is widely used as a proxy for volcanic activity in the geological record, as the primary natural source of Hg in the environment is volcanism (e.g., Grasby et al., 2019). Volcanic Hg undergoes global transport due to its residence time of ca. 0.5–1 years in the atmosphere, prior to its deposition into terrestrial and marine sediments via wet and dry pathways (Selin, 2009; Gworek et al., 2016). Mercury has a strong bond to organic matter, often resulting in a fairly stable Hg/TOC ratio in sediments (e.g., Grasby et al., 2013, 2019). During intense volcanic activity, such as LIP eruptions, Hg flux to the environment is expected to be largely enhanced and result in anomalous Hg enrichment in sediments globally (e.g., Grasby et al., 2020). Evidence of such enrichments has been highlighted in multiple instances in the geological record, e.g., the end-Permian and end-Triassic mass extinctions (Grasby et al., 2019; Yager et al., 2021).

Besides the amount of Hg in sedimentary rocks, Hg isotopes can be used to understand the geochemical fate of Hg in the en-

vironment (Grasby et al., 2017). Mercury has seven natural stable isotopes (^{196}Hg, ^{198}Hg, ^{199}Hg, ^{200}Hg, ^{201}Hg, ^{202}Hg, and ^{204}Hg) that undergo unique mass-dependent Fractionation (MDF, i.e., δ^{202}Hg) and mass-independent Fractionation (odd-MIF, i.e., Δ^{199}Hg) (e.g., Blum et al., 2014). Volcanogenic Hg normally has $\Delta^{199}\text{Hg} \approx 0$ (Yin et al., 2016) and therefore the input of large amounts of volcanogenic Hg can lead to shifts in Δ^{199}Hg in sediments. Shifts in Δ^{199}Hg have been highlighted at some of the largest mass extinctions, strengthening the link between extinctions and massive volcanic eruptions (e.g., Bergquist, 2017; Grasby et al., 2017, 2019; Shen et al., 2019; Yager et al., 2021). The Hg isotope record from the marine Upper Triassic of the South China Block of eastern Tethys displays overall negative Δ^{199}Hg values associated with some positive Δ^{199}Hg values around the CPE time, further indicating enhanced volcanogenic Hg input into the ocean via atmospheric Hg deposition and terrestrial erosion (Zhao et al., 2022).

LIP eruptions are a stochastic process with pulses of variable eruption intensity, as shown by high-resolution radioisotope age dates of the Deccan Traps (Schoene et al., 2019), and which can be described as a binomial multiplicative cascade (e.g., Gusev, 2014). Given this Grasby et al. (2020) modeled volatile release from a LIP event as a multifractal time series, with peak emission rates being able to induce conditions toxic to marine and terrestrial life. Consistent with this, carbon-isotope and Hg records suggest that volcanic activity at the CPE occurred in multiple pulses (Dal Corso et al., 2018; Lu et al., 2021). Understanding whether some of these eruptive pulses at the CPE may have been particularly intense may help illuminate the links between Wrangellia volcanism, the associated emission of greenhouse gases and other potential environmental pollutants, and the climate and biotic changes coincident with the CPE.

We here present a Hg concentration and isotope ratio record from a pelagic deep-water section (Section N-O, Inuyama, Japan). The section, located in the Panthalassic Ocean during the Carnian (Fig. 1B), is well constrained by conodont and radiolarian biostratigraphy (Yamashita et al., 2018; Tomimatsu et al., 2021, 2022). This particular paleogeographic position makes the Japanese record less sensitive to terrestrial input and therefore more suitable for retrieving reliable information on volcanic activity associated with the CPE.

2. Geological setting and studied section

Section N-O, located in the Inuyama area, Mino Belt, central Japan (Fig. 1B, C), is a composite stratigraphic section that is comprised of Sections N and O (Sugiyama, 1977; Tomimatsu et al., 2021). The Mino Belt consists of a Jurassic subduction-generated accretionary complex striking in an approximately ENE–WSW orientation. Based on lithology, age, and structure, the Mino Belt has been divided into six tectonostratigraphic units: Sakamoto-toge, Samondake, Funabuseyama, Nabi, Kanayama, and Kamiaso (Wakita, 1988). The examined sections are located in the Kamiaso unit (Wakita, 1988), which is composed of thrust sheets of sedimentary successions including Triassic to Lower Jurassic bedded cherts and overlying Middle Jurassic sandstones and mudstones (Fig. 1D; Matsuoka, 1994). Paleomagnetic and biostratigraphic investigations of bedded cherts in the Inuyama area revealed that deposition occurred in the central Panthalassa during the Triassic and it shifted from low to mid-latitudes during the Middle Triassic to Early Jurassic (Ando et al., 2001; Uno et al., 2012). The chert-clastic sequence in the Inuyama area has been subdivided into four chert thrust sheets: CH-1, CH-2, CH-3, and CH-4, with no carbonate or terrigenous rocks (e.g., Matsuda and Isozaki, 1991).

Section N-O is within the CH-2 thrust sheet and is a ~18 m thick succession composed of red cherts and greenish gray cherts with interbedded white cherts (Fig. 2). The bedded cherts are intercalated with thin siliceous claystone. The section was dated as Late Ladinian to Late Carnian based on radiolarians and conodonts biostratigraphy (Yamashita et al., 2018; Tomimatsu et al., 2021, 2022). The boundary between Julian 1 and 2 (the onset of the CPE, e.g., Dal Corso et al., 2018) was defined by the first occurrence of *Paragondolella praelindae* conodont Zone (Rigo et al., 2007, 2018) and TR4B radiolarian Zone (Fig. 2; Tomimatsu et al., 2021). Thermal maturity studies indicate that the bedded chert in the Inuyama area has not been buried below the depth of the prehnite-pumpellyite facies (Matsuda and Isozaki, 1991), suggesting that the Carnian rocks in the Section N-O have not been affected by hydrothermal-metasomatic alteration.

High-resolution Os isotope data were obtained from the bedded cherts, showing a decrease in ^{187}Os/^{188}Os ratios in the Julian 1, which remains constantly low throughout the Julian 2. This was attributed to the increased input of unradiogenic Os into the ocean caused by the emplacement of the Wrangellia LIP (Fig. 2; Tomimatsu et al., 2021). Two negative carbon-isotope excursions (NCIE-α and -β) of organic matter were documented in the siliceous claystone and can be correlated globally (Fig. 2; Tomimatsu et al., 2021). Furthermore, the NCIE-β interval was also characterized by dysoxic to anoxic conditions based on the enrichments of V and U, suggesting worldwide ocean anoxia during the CPE (Fig. 2; Tomimatsu et al., 2021).

3. Material and methods

In this study, we selected 23 siliceous claystone beds for the analyses of major and trace elements, Hg concentrations, and 20 samples for Hg isotopes. Major elements analysis was performed at the ALS Chemex, Guangzhou, China by using X-ray fluorescence spectroscopy (PANalytical XRF) in accordance with the ME-XRF26 analytical package. Each sample was well mixed with the flux made of lithium tetraborate and lithium nitrate, and then was heated to 1050 °C. The slurry was moved into a platinum mold, which was then cooled to form a sheet. The analytical uncertainty was <5%.

Trace element concentrations were measured using an Agilent 8900 inductively-coupled plasma–mass spectrometry (ICP–MS) at the Institute of Geochemistry, Chinese Academy of Sciences (IGCAS), following a previous method (Liang and Grégoire, 2000). The analytical uncertainty was <5% for the elements reported. Hg concentrations were measured using a Lumex R915+ mercury analyzer at the Institute of Geochemistry, Chinese Academy of Sciences (IGCAS), Guiyang, China. Approximately 150 mg of powder was weighed for each sample. Sample duplicates (1 replication sample for every 10 samples) and soil standard reference material (SRM, GSS-5, 290 ppb Hg) were included in the analysis, which yielded Hg recoveries of 90-110% for GSS-5 and uncertainty of <10% for sample duplicates.

The samples were processed for Hg preconcentration using a double-stage tube furnace (Zerkle et al., 2020). GSS-4 soil SRM (n=3) was prepared in the same way as the samples. The preconcentrated solutions, in 5 mL 40% anti aqua regia (HNO_3/HCl = 2/1, v/v), were diluted to 1.0 ng/mL, with an acid concentration of 10–20% by using 18.2 MΩ cm water, and then analyzed using Neptune Plus Multicollector-Inductively Coupled Plasma Mass Spectrometer (Thermo Electron Corp, Bremen, Germany) at IGCAS (Yin et al., 2016). MDF of Hg isotopes is expressed in δ^{202}Hg notation in units of per mil (‰) referenced to the NIST-3133 Hg standard before and after each sample, as follows:

$$\delta^{202}\text{Hg} = [(^{202}\text{Hg}/^{198}\text{Hg}_{\text{sample}})/(^{202}\text{Hg}/^{198}\text{Hg}_{\text{standard}}) - 1] \times 1000 \quad (1)$$

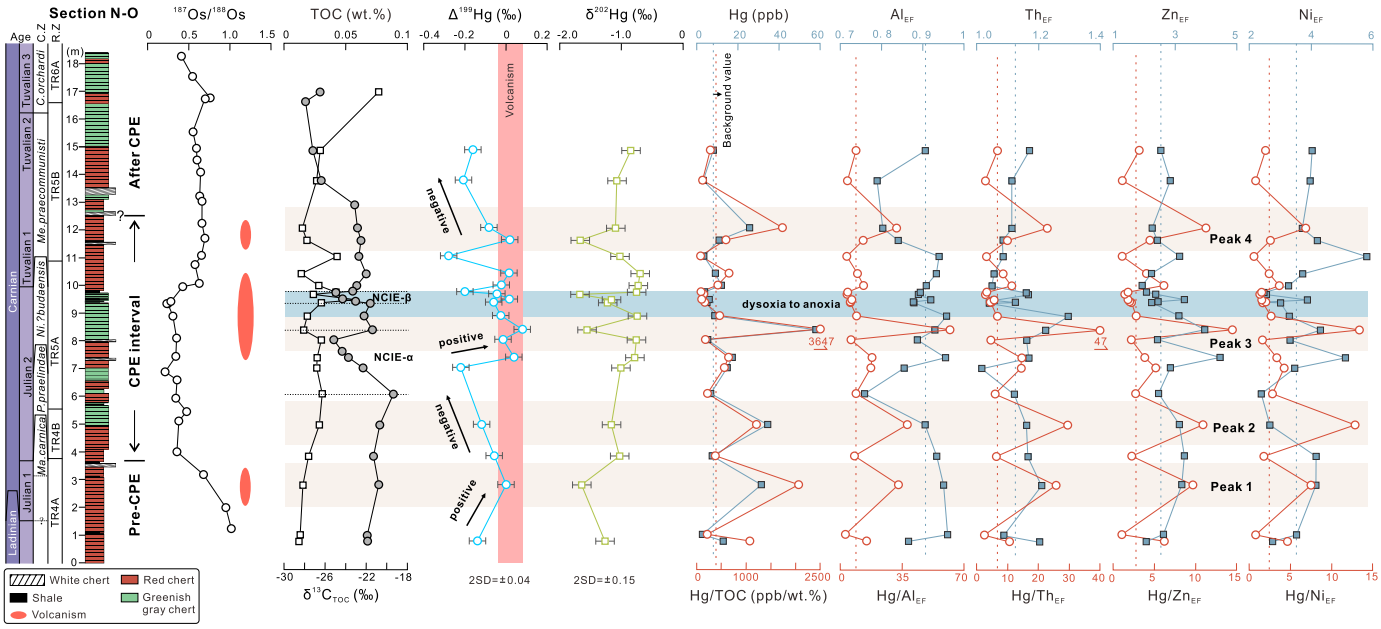

Fig. 2. Lithostratigraphic log, Os isotopes, organic carbon isotopes ($\delta^{13}C_{TOC}$), total organic carbon (TOC), Hg concentrations, $\Delta^{199}Hg$, $\delta^{202}Hg$, ratios of Hg to TOC, Al_{EF}, Th_{EF}, Zn_{EF} and Ni_{EF} (EF = enrichment factor) of siliceous claystones in Section N-O (Inuyama, Japan). Lithostratigraphy, biostratigraphy, Os isotopes, $\delta^{13}C_{TOC}$, TOC and inferred interval of dysoxia to anoxia (pastel blue belt) are from Tomimatsu et al. (2021). Interval in $\Delta^{199}Hg$ values that are indicative of volcanogenic Hg input according to Shen et al. (2022a) is marked by vertical pink rectangle. Background values are the median values and marked as steel blue dashed lines (concentrations) and crimson dashed lines (ratios). NCIE = negative carbon-isotope excursion; CPE = Carnian Pluvial Episode; C.Z = Conodont zone; R.Z = Radiolarian zone. *Ma. carnica* = *Mazzaella carnica*; *P. praelindae* = *Paragondolella praelindae*; *Ni.? budaensis* = *Nicoraella budaensis*; *Me. praecommunisti* = *Metapolygnathus praecommunisti*; *C. orchardi* = *Carnepigondolella orchardi*.

MIF of Hg isotopes is reported in Δ notation ($\Delta^{xxx}Hg$), which describes the difference between the measured $\delta^{xxx}Hg$ and the theoretically predicted $\delta^{xxx}Hg$ values, in units of per mille (‰), using the following Equation:

$$\Delta^{xxx}Hg \approx \delta^{xxx}Hg - \delta^{202}Hg \times \beta \quad (2)$$

where β value is 0.252 for ^{199}Hg, 0.5024 for ^{200}Hg, and 0.752 for ^{201}Hg, respectively (Blum and Bergquist, 2007). NIST-8610 secondary Hg standard solution, diluted to 1.0 ng/mL Hg in 10% HCl, was measured in the same way as the samples. The overall average and uncertainty of GSS-4 ($\delta^{199}Hg$: −0.83±0.07‰; $\delta^{200}Hg$: −0.86±0.10‰; $\delta^{201}Hg$: −1.65±0.13‰; $\delta^{202}Hg$: −1.71±0.15‰; $\Delta^{199}Hg$: −0.40±0.04‰; $\Delta^{200}Hg$: 0.00±0.03‰; $\Delta^{201}Hg$: −0.36±0.05‰, 2SD, n=3) and NIST-8610 ($\delta^{199}Hg$: −0.14±0.05‰; $\delta^{200}Hg$: −0.25±0.03‰; $\delta^{201}Hg$: −0.39±0.04‰; $\delta^{202}Hg$: −0.50±0.02‰; $\Delta^{199}Hg$: −0.02±0.04‰; $\Delta^{200}Hg$: 0.00±0.03‰; $\Delta^{201}Hg$: −0.01±0.04‰, 2SD, n=3) agree well with previous results (e.g., Blum and Bergquist, 2007; Deng et al., 2021). Analytical uncertainty reported in this study corresponds to the larger value of replicate analyses of GSS-4 and NIST-8610.

4. Results

To eliminate the considerable dilution effect of biogenic silica (e.g., Tomimatsu et al., 2021; Cho et al., 2022), elements (e.g., Al, Th, Zn, Cu, Ni, V, U) were normalized to Ti concentrations to obtain enrichment factors which are defined as: $X_{EF} = (X_{sample}/Ti_{sample})/(X_{UCC}/Ti_{UCC})$, where X and Ti represent the weight concentrations of elements X and Ti, respectively. Samples were normalized using upper continental crust (UCC) compositions of Rudnick and Gao (2014).

The Hg concentrations of the pelagic siliceous claystone in Section N-O range from 3 to 58 ppb, with a mean value of 13 ppb (N=23). Four peaks in Hg concentrations above the background value are observed. The first Hg peak (Max. = 31 ppb; Peak 1 in Fig. 2) at ~2.8 m, prior to the NCIE-α of Tomimatsu et al. (2021) and the CPE interval, is approximately four-fold higher than the background value (median value of Hg concentrations, 8 ppb; Fig. 2) and coincides with the first peak of Hg/TOC (2056 ppb/wt.%), Hg/Al_{EF} (33), Hg/Th_{EF} (26), Hg/Zn_{EF} (10), Hg/Ni_{EF} (8) ratios (Fig. 2). The second Hg peak (Max. = 34) at ~5.0 m and within the lower part of Julian 2, still precedes the NCIE-α, and is coincident with the second peak in the ratios of Hg/TOC (1208 ppb/wt.%), Hg/Al_{EF} (38), Hg/Th_{EF} (30), Hg/Zn_{EF} (11), Hg/Ni_{EF} (13) (Fig. 2). The third peak of Hg concentrations (up to 58 ppb in Fig. 2) at ~8.4 m of the section almost overlaps with NCIE-α. The ratios of Hg/TOC (3647 ppb/wt.%), Hg/Al_{EF} (62), Hg/Th_{EF} (47), Hg/Zn_{EF} (15), and Hg/Ni_{EF} (13), also culminated at the same level in Section N-O. Up section (~9 to 11 m), overlapping with the NCIE-β interval, Hg concentrations are broadly stable and are close to the background value. The fourth peak (Peak 4) of Hg concentrations (26 ppb) at ~12 m, after the CPE NCIEs but may still within the CPE interval, is also coincident with a peak in Hg/TOC (1731 ppb/wt.%), Hg/Al_{EF} (32), Hg/Th_{EF} (23), Hg/Zn_{EF} (11), and Hg/Ni_{EF} (7) ratios (Fig. 2).

$\Delta^{199}Hg$ values have a wide range and vary between −0.28‰ and 0.08‰, with an average of −0.07±0.04‰ (2SD, n=20). $\Delta^{199}Hg$ values are near-zero during the first peak in ratios of Hg/TOC (2056 ppb/wt.%), Hg/Al_{EF} (33), Hg/Th_{EF} (26), Hg/Zn_{EF} (10), and Hg/Ni_{EF} (8); and $\Delta^{199}Hg$ then shows a negative shift to −0.22‰ prior to the most negative values of NCIE-α. A positive shift in $\Delta^{199}Hg$ is observed within NCIE-α, and then $\Delta^{199}Hg$ values are consistently close to zero from 7.4 to 12.1 m (the upper part of the CPE interval in the Fig. 2), except for two negative values (−0.20‰ and −0.28‰) at 9.8 m and 11.1 m respectively. This interval (7.4 to 12.1 m) also brackets the most negative values of the NCIE-α and the whole of NCIE-β, as well as the dysoxic to anoxic interval and the maximum values in Hg concentrations and Cu_{EF}/V_{EF} ratios of the claystones and cherts (Figs. 2 and 3).

After the CPE interval, $\Delta^{199}Hg$ values decrease to −0.21±0.04‰ at 13.8 m (Fig. 2). $\delta^{202}Hg$ values are negative, with an average of −1.10±0.15‰ (2SD, N=20), throughout Section N-O (Fig. 2).

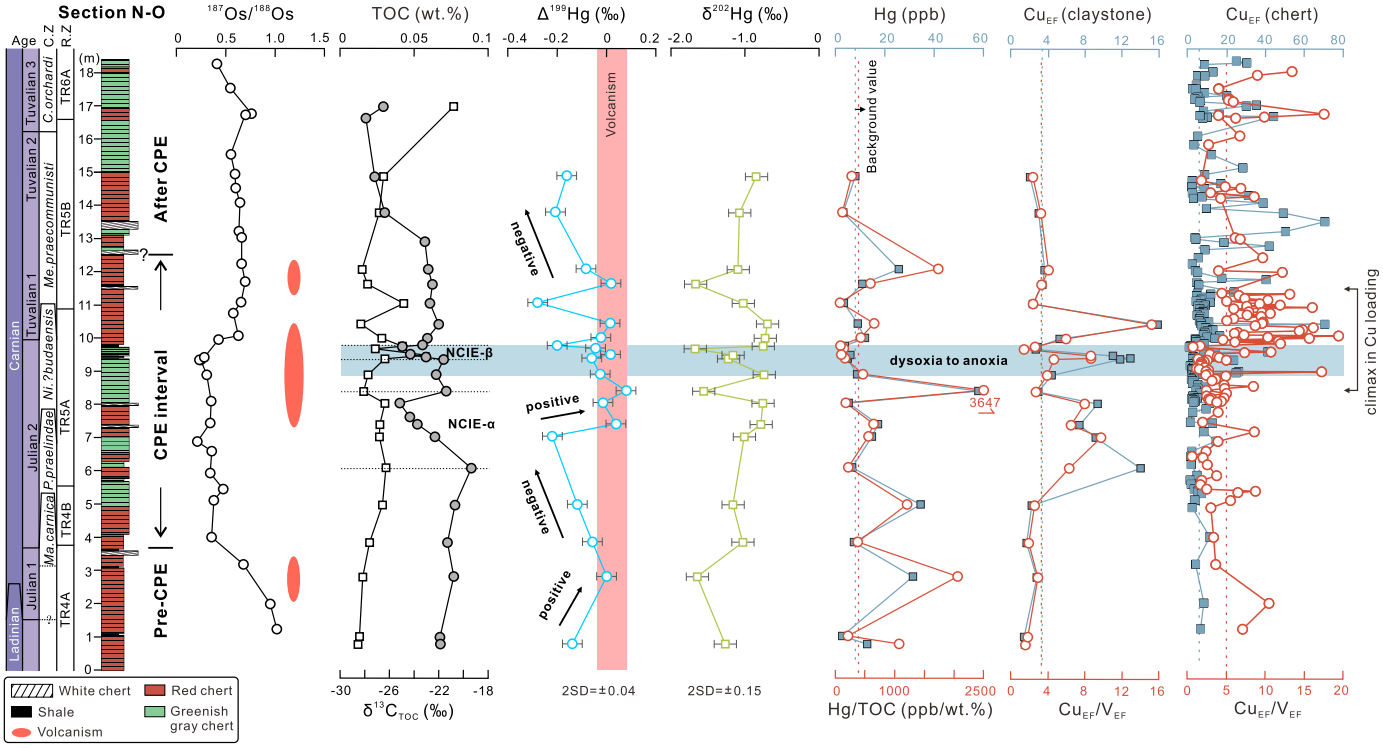

Fig. 3. Litho-biostratigraphy, Os isotopes, organic carbon isotopes ($\delta^{13}C_{TOC}$), total organic carbon (TOC), Hg concentrations, Hg/TOC ratios, $\Delta^{199}Hg$, $\delta^{202}Hg$, Cu_{EF} and Cu_{EF}/V_{EF} ratios from claystone and chert in Section N-O. Litho-biostratigraphy, $\delta^{13}C_{TOC}$, TOC, Os isotopes, inferred interval of dysoxia to anoxia (pastel blue belt), Cu_{EF} and Cu_{EF}/V_{EF} ratios (normalized to Ti concentrations) of chert are from Tomimatsu et al. (2021). Interval in $\Delta^{199}Hg$ values that are indicative of volcanogenic Hg input according to Shen et al. (2022a) are marked by a vertical pink rectangle. Background values are the median values and marked as steel blue dashed lines (concentrations) and crimson dashed lines (ratios) in this study. The abbreviations of conodont and radiolarian zones are shown in Fig. 2.

5. Discussion

5.1. Primary control on Hg accumulation in Section N-O

Organic matter is usually the host phase of Hg in sediments, which is reflected by a strong positive correlation between Hg and TOC (e.g., Grasby et al., 2013, 2019; Shen et al., 2019 and reference therein). Consequently, high Hg concentrations and high Hg/TOC ratios found in sediments may indicate an increase in Hg influx from an external source, such as volcanism (e.g., Grasby et al., 2019; Shen et al., 2019 and reference therein). However, normalization with TOC values < 0.2 wt.% may produce artificial Hg/TOC spikes (Grasby et al., 2019).

In Section N-O, Hg and TOC show no correlation (r=-0.35, p=0.11; Fig. 4), and the TOC values are constantly low, with an average TOC value of ~0.03 wt.% (reported in Tomimatsu et al., 2021; also seen in Fig. 2). This suggests that the organic matter deposition did not exert a major control on Hg accumulation, and the peaks (1 to 4) in Hg/TOC ratios indicate that Hg enrichment can not be linked to increased abundance in organic matter (Fig. 4). Clay minerals can also host Hg owing to their high surface area reactivity (e.g., Kongchum et al., 2011; Jin et al., 2022b). Al and Th are elements that are used to assess the clay fraction abundance in the sediments, as well as pelagic rocks (e.g., Grasby et al., 2019; Shen et al., 2019, 2022a and references therein). At Section N-O, they both exhibit no covariation with Hg concentrations (r=0.14, p=0.52; r=0.35, p=0.10; Fig. 4), indicating clay minerals are not the main host phase of Hg.

Also S or sulfides (e.g., Zn- and Ni- sulfides; Jin et al., 2022b; Shen et al., 2022a,b) can host Hg. The S concentrations in analyzed samples, however, are below the 0.1 wt.% detection limit, and therefore S was not considered in this study. Furthermore, Ni and Zn (Jin et al., 2022b), have no or moderate correlation (r=0.17, p=0.44; r=0.47, p=0.02, respectively) with Hg concentrations (Fig. 4), indicating that Hg accumulation may be only limitedly linked to sulfides abundance.

Redox condition and pyrite formation may have influenced the Hg record (e.g., Shen et al., 2019, 2022b). V and U are easily formed to insoluble chemical precipitate in anoxic and/or euxinic bottom water (e.g., Algeo and Maynard, 2004). Therefore, the enrichment factors of V and U (e.g., V_{EF} and U_{EF}) are used as proxy for redox conditions (e.g., Tomimatsu et al., 2021). In Section N-O, V_{EF} and U_{EF} abruptly increase in the late Julian 2 in the studied section (see figure 3 in Tomimatsu et al., 2021), suggesting dysoxic to anoxic conditions (Fig. 2). Peaks in Hg concentrations highlighted by our study, however, do not coincide with that reducing interval (Fig. 2), and the V_{EF}, U_{EF} and sulfide-enriched elements (Ni) have no correlation (except for Zn) with Hg values (Fig. 4). This suggests that redox conditions did not exert strong control on Hg enrichment at Section N-O.

Changes in lithological composition, grain size, sedimentation rates, and depositional conditions could influence Hg accumulation too (Moore et al., 2019; Them et al., 2019; Yager et al., 2021). In Section N-O, Hg concentrations were obtained exclusively from claystones, thus minimizing the possible effect due to sampling of rocks with different grain size. There is no evidence of large changes in sedimentation rates at Section N-O. This is in line with the fact that the section is pelagic and therefore significant variations in sediment supply are not expected. Therefore, Hg peaks observed at Section N-O are likely independent of sedimentation rate.

Post-depositional alteration of Hg deposition in the marine sediments is an on-going debate. Gobeil et al. (1999) provided evidence of redox-driven Hg redistribution, however this scenario seems unlikely in Section N-O because there is no coincidence between Hg peaks and the interval characterized by anoxic/dysoxic

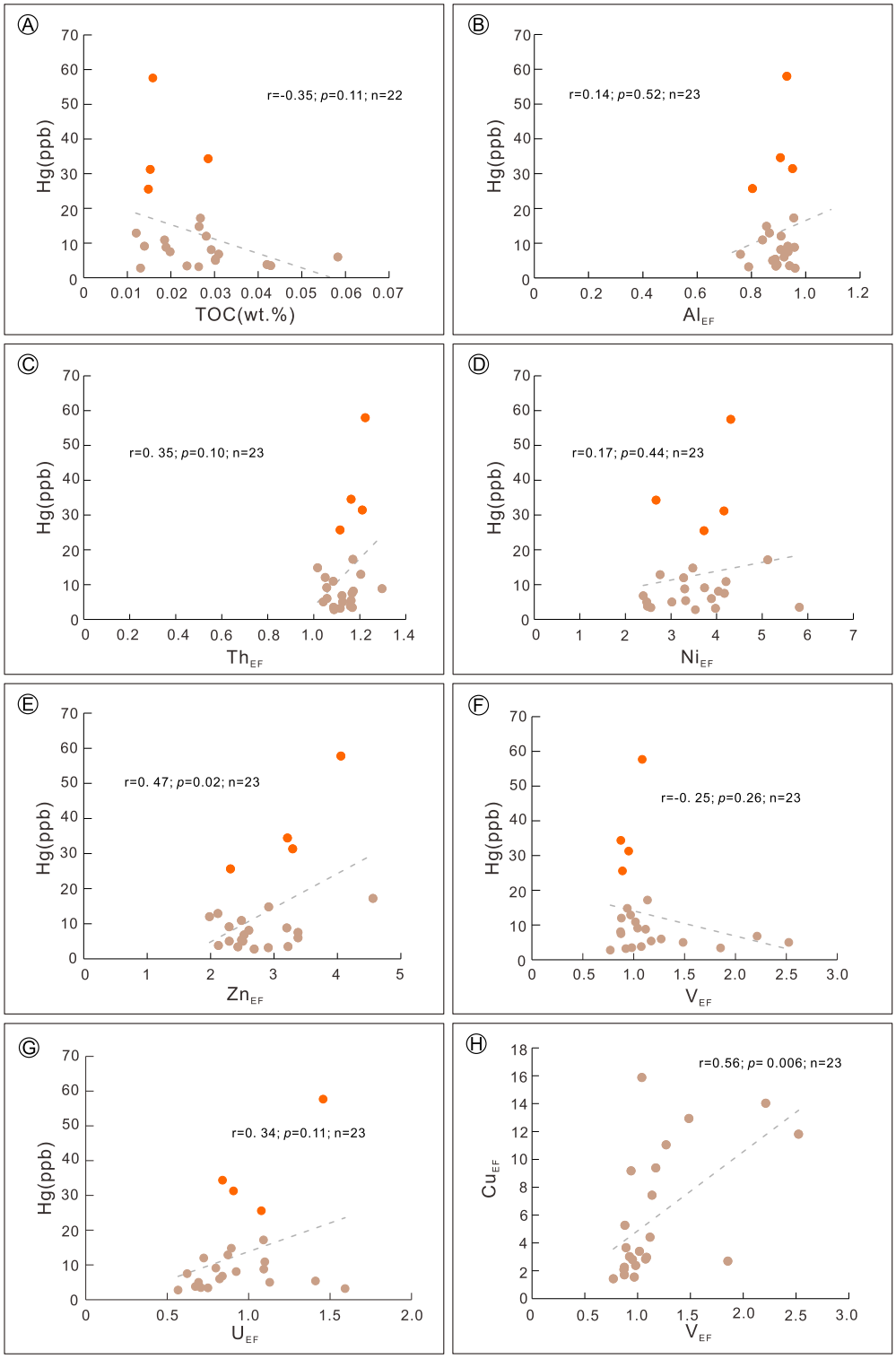

Fig. 4. A) plot of Hg vs TOC; B) plot of Hg vs Al_{EF}; C) plot of Hg vs Th_{EF}; D) plot of Hg vs Ni_{EF}; E) plot of Hg vs Zn_{EF}; F) plot of Hg vs V_{EF}; G) plot of Hg vs U_{EF}; H) plot of Cu_{EF} vs V_{EF}. Orange symbols indicate samples are characterized by highest Hg concentrations within the four peak intervals (see in Fig. 2). EF=Enrichment Factor.

conditions (Fig. 2), In addition, no clear correlation has been found between concentrations of Hg and redox-sensitive elements (Fig. 4; see discussion above). A recent study on Hg accumulation from the Western Mediterranean abyssal plain, revealed that mercury had a strong association with sulfur but a poor relationship with the Fe cycle, suggesting that diagenetic remobilization had minimal impact on Hg's vertical distribution (Cossa et al., 2021).

In summary, Hg concentrations in Section N-O exhibit non-significant covariation with TOC, Al_{EF}, Th_{EF}, Ni_{EF}, V_{EF} and U_{EF}, and a moderate correlation with Zn_{EF} (Fig. 4), and seem to not be influenced by changes in sedimentation rates, depositional conditions, or by post-depositional alterations. The co-occurring peaks (1-4 in Fig. 2) in Hg concentrations, Hg/TOC, Hg/Al_{EF}, Hg/Th_{EF}, Hg/Zn_{EF}, Hg/Ni_{EF} ratios throughout Carnian successions of Section N-O im-

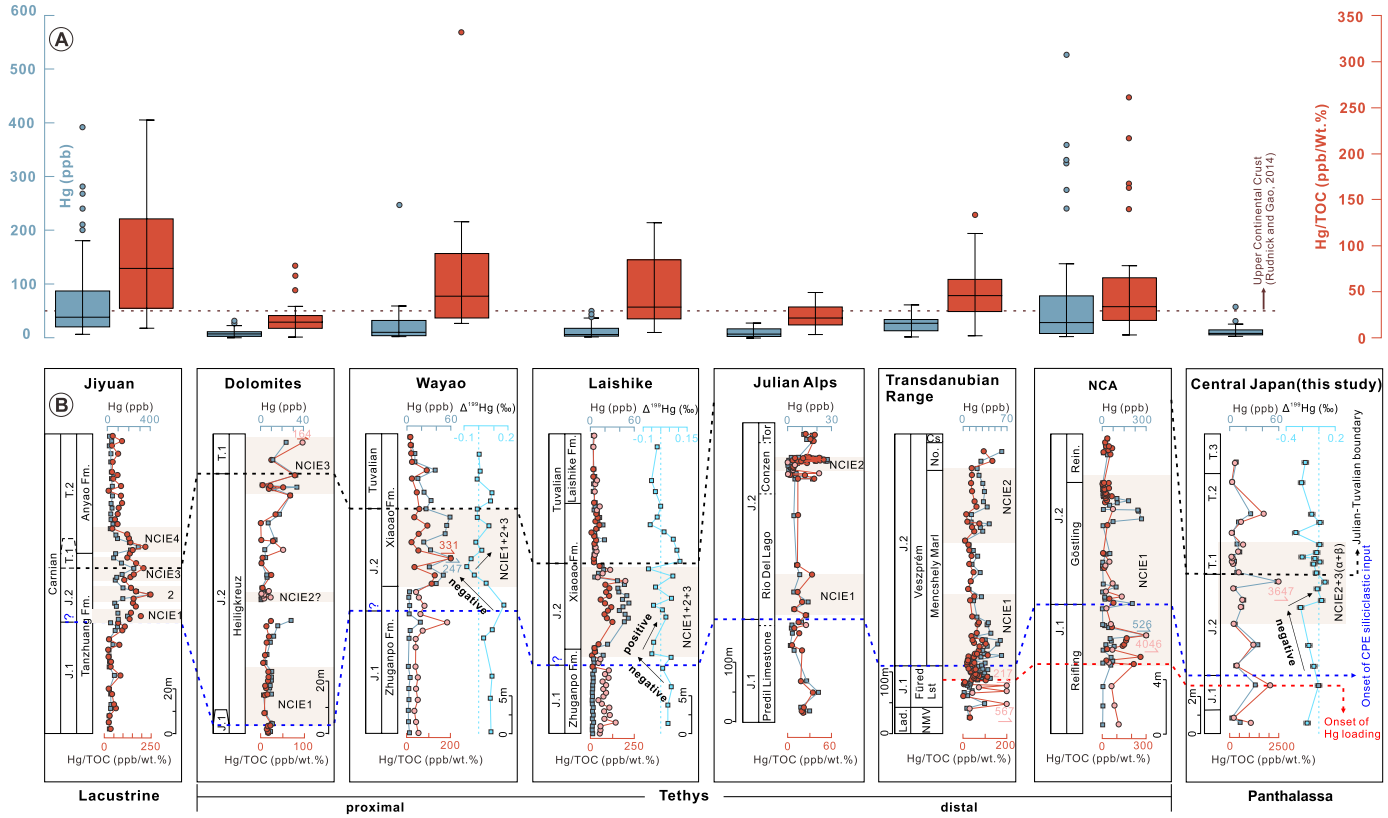

Fig. 5. Carnian Hg records are shown in bar and whisker plots (A) and in stratigraphic order followed the depositional profile (B): Jiyuan Basin (lacustrine, North China; Lu et al., 2021), marine successions of Alpine region (Dolomites, Julian Alps, Transdanubian Range, Northern Calcareous Alps; Mazaheri-Johari et al., 2021), marine successions of South China (Wayao and Laishike; Zhao et al., 2022) and central Japan (Panthalassic Ocean; this study). J.1 = Julian 1; J.2 = Julian 2; T.1 = Tuvalian1; T.2 = Tuvalian 2; T.3 = Tuvalian 3; NCA = Northern Calcareous Alps; No. = Nosztor Limestone; Cs. = Csicsó Marl; Rein. = Reingraben Formation. The vertical pastel blue dashed lines in the Δ^{199}Hg columns represent volcanic Hg(0) isotopic signal (Δ^{199}Hg = ~ 0‰) (e.g., Yin et al., 2016). The pink dots in the sections show the uncertainties in Hg/TOC values (TOC < 0.2 wt.%). Note: The crimson boxes in A do not include Hg/TOC values which TOC are less than 0.2 wt.%.

ply enhanced Hg loading from an external source, and it is reasonable to identify this source as volcanism.

5.2. Comparison of Hg and Hg/TOC records at the CPE

All published Hg data across the CPE, from continental and marine basinal successions, are summarized in Fig. 5 (data from Lu et al., 2021; Mazaheri-Johari et al., 2021; Zhao et al., 2022; this study). In the figure we define "proximal" and "distal" successions of the Tethyan domain with respect to their relative distance from shoreline, closer (proximal) and farther (distal).

Overall, the majority of published data from Carnian successions have Hg concentrations that are lower than ~50 ppb, the average value of the upper continental crust (Fig. 5; Rudnick and Gao, 2014), and ~65 ppb, the average Hg concentrations in sedimentary rocks (Grasby et al., 2019). Lacustrine records (Jiyuan Basin) have both high Hg concentrations (avg. = 71 ppb) and Hg/TOC ratios (avg. = 85 ppb/wt.%). Distal successions generally display lower Hg concentrations than the proximal ones, as may be expected and in line with findings of Grasby et al. (2017) and Them et al. (2019), because proximal settings would receive more Hg inputs from rivers. However, among the areas considered in this study, the Dolomites succession, which is the most proximal to land, has the lowest average Hg concentrations and Hg/TOC. This apparent contradiction could be due to local variability or to the difference in sedimentation rates among the various locations. Another counterintuitive aspect of the Hg and Hg/TOC records in Fig. 5 is that marine distal sections (e.g., NCA and the Transdanubian Range) show a significant increase in Hg/TOC at the onset of NCIE 1 that is not observed in proximal locations (e.g., Dolomites and Laishike). Mazaheri-Johari et al. (2021) pointed out that variations in Hg concentrations and position and magnitude of the Hg/TOC spikes in the Tethyan successions may be related to low sampling resolution that did not fully capture the Hg enrichment horizons.

Since deeper water settings are far from continental influences and sedimentation, and although slow, tend to be steadier, it is reasonable to consider that they record variations in atmospheric Hg loading more faithfully (e.g., Grasby et al., 2017; Wang et al., 2018). It is therefore interesting to compare deep water Hg records from the Transdanubian Range and NCA with data from Section N-O (Panthalassa). In these three deep water successions, evidence of enhanced Hg flux starts in the Julian 1 (Fig. 5). Hg/TOC enrichments from the Transdanubian Range and NCA are up to 113 ppb/wt.% and 261 ppb/wt.%, respectively and the Julian 1 portion of Section N-O shows relatively high Hg and Hg/TOC and yields near-zero Δ^{199}Hg (Figs. 2 and 5). Such evidence is consistent with onset of Wrangellia volcanism in Julian 1, prior to the Julian 1/Julian 2 boundary and therefore preceding the increase in siliciclastic input and carbonate crisis that marks the onset of the CPE (Fig. 5; e.g., Breda et al., 2009; Dal Corso et al., 2018). This observation is further consistent with a mantle-derived influx of unradiogenic Os indicated by a decrease in ^{187}Os/^{186}Os ratios in Julian 1 (Fig. 2; Tomimatsu et al., 2021).

5.3. Hg isotope signatures in Section N-O record climax in Wrangellia LIP volcanism

Hg-MIF (i.e., Δ^{199}Hg) is predominantly produced by photoreduction of Hg^{2+} to gaseous Hg^0 during atmospheric transport, resulting in positive Δ^{199}Hg in the atmospheric Hg (II) species

and negative Δ^{199}Hg in the gaseous Hg^0 (Bergquist and Blum, 2007; Blum et al., 2014). Wet deposition of atmospheric Hg (II) (e.g., through rainfall) causes positive Δ^{199}Hg in the seawater (Thibodeau and Bergquist, 2017). In contrast, soil and vegetation have negative Δ^{199}Hg values because they preferentially capture gaseous Hg^0 (Bergquist and Blum, 2007; Blum et al., 2014). When plants uptake Hg, this results in negative Δ^{199}Hg vegetation signatures (Bergquist and Blum, 2007). Photoreduction of mercury (e.g., Hg^{2+} and MeHg) in aqueous environment leads to $\Delta^{199}Hg/\Delta^{201}Hg$ exhibiting a linear relationship of 1 to 1.3 (Bergquist and Blum, 2007; Yin et al., 2016), as observed in Section N-O (slope=1.2; Fig. S1 in supplemental information). Mercury also undergoes photochemical reduction during long periods of atmospheric transport. This phenomenon imparts a positive Δ^{199}Hg signature. Distal settings, far from continental influence, tend to be mainly supplied by atmospheric Hg and therefore sediments display more positive Δ^{199}Hg values than proximal areas (e.g., Bergquist and Blum, 2007; Grasby et al., 2017). In contrast, Hg-MDF (δ^{202}Hg) can result from numerous biological, abiotic chemical and physical processes (Blum et al., 2014; Grasby et al., 2017), making it difficult to distinguish Hg source by using δ^{202}Hg alone. During major volcanic events, volcanogenic Hg is emitted in large quantities and therefore can dominate total Hg in sediment (Grasby et al., 2020), resulting in near-zero Δ^{199}Hg values (e.g., Grasby et al., 2019; Shen et al., 2019).

Given the above, we interpret the Δ^{199}Hg record of Section N-O as follows. In the Ladinian portion of Section N-O Δ^{199}Hg values are negative (-0.14 ± 0.04‰; Figs. 2 and 3), suggesting a dominantly terrestrially sourced background Hg flux. However, the Δ^{199}Hg shifts to a more positive value (0.00 ± 0.04‰) in the Julian 1, coincident with Peak 1 in Hg concentrations, Hg/TOC, Hg/Al_{EF}, Hg/Th_{EF}, Hg/Zn_{EF}, and Hg/Ni_{EF} ratios (Fig. 2). These more positive Δ^{199}Hg values suggest increased volcanogenic Hg flux, in agreement with the evidence of unradiogenic Os input reported by Tomimatsu et al. (2021), as shown in Fig. 2, and interpreted as being connected to Wrangellia LIP activity. The timing of the positive Δ^{199}Hg shift precedes the onset of the CPE which is marked by siliciclastic input dated to the Julian 1/Julian 2 boundary (Fig. 5; e.g., Breda et al., 2009; Dal Corso et al., 2018). These observations further support the hypothesis that Wrangellia volcanism had started before the CPE (see discussion in 5.2).

Within Julian 2, Δ^{199}Hg values then display a negative trend, shifting from 0 to -0.22 ± 0.04‰. Such a negative shift is suggestive of a strong increase in terrestrial Hg flux in agreement with evidence for a global increase in runoff and terrigenous supply, which is one of the main sedimentological features of the CPE in many marine settings from proximal to pelagic (e.g., Breda et al., 2009; Cho et al., 2022). Negative Δ^{199}Hg shifts in the shallow marine successions of Laishike and Wayao sections are consistent with such evidence (Fig. 5; Zhao et al., 2022). These localities belong to the shallow water Tethyan domain and occupied a paleogeographic location that was thousands of kilometers from the Section N-O in the Late Triassic (Fig. 1B), implying that the Δ^{199}Hg negative trend is not a local feature.

The Δ^{199}Hg at Section N-O then rises, reaching near-zero values in the upper Julian 2 portion of the section, and then oscillates around zero across the Julian/Tuvalian boundary. A similar trend is again observed at Wayao and Laishike. Such a prolonged stratigraphic interval with near-zero Δ^{199}Hg suggests that this was a phase of particularly intense and continuous activity of the Wrangellia LIP. The above evidence is consistent with the fractal nature of LIP events suggested by models (Grasby et al., 2020) where periods of particularly intense eruptive activity would be expected during the emplacement volcanic products.

Further interesting insights come from the observation of the record of Cu Enrichment Factor (Cu_{EF}) in cherts and claystones across the Julian/Tuvalian transition at Section N-O (Fig. 3). Cu is a volatile metal that is released from the magma and can exert detrimental effects to both the marine and terrestrial systems (e.g., Grasby et al., 2020; Chu et al., 2021; Zhang et al., 2021). Volcanic aerosols with Cu particles can be transported for long distances, analogous to Hg (e.g., Zhang et al., 2021), and also Cu usually accumulates as sulphides in reducing environments and/or is easily adsorbed onto organic matter (e.g., Dolenec et al., 2001; Shen et al., 2022b).

There is no relationship between Cu_{EF} and TOC, Zn_{EF}, Ni_{EF}, or U_{EF} (Fig. S2 in supplemental information), but there is a strong moderate correlation between Cu_{EF} and V_{EF} ($r=0.56$, $p=0.006$; Fig. 4), indicating that the Cu is not hosted by organic matter, but it may be partly controlled by reducing conditions in the ocean. However, after normalization to V_{EF}, peaks in Cu_{EF}/V_{EF} are still present and coincide with those in Cu_{EF} at or close to the Julian/Tuvalian boundary (Fig. 3). Such maxima in Cu_{EF}/V_{EF} and Cu_{EF} may therefore be indicative of enhanced volcanism and are consistent with evidence from Hg concentrations. Furthermore they coincide with the interval with near-zero Δ^{199}Hg values.

Notably, within the overall interval of near-zero Δ^{199}Hg values that characterizes the upper Julian/lower Tuvalian, two minimums in Δ^{199}Hg values can be observed in Section N-O (~9.8 m and 11.1 m). Such minima follow Peak 3 in Hg concentrations and coincide with NCIE-β in the section's $\delta^{13}C_{TOC}$ record (Figs. 2 and 3) which occur at the Julian/Tuvalian transition and have been correlated to the third negative shift in δ^{13}C of the CPE δ^{13}C in the Western Tethys (Fig. 1; Tomimatsu et al., 2021). A potential concurrent factor driving the negative Δ^{199}Hg values could be photoreduction of Hg^{2+} complexed by reduced sulfur ligands in euxinic conditions (e.g., Shen et al., 2022a). This would agree with the evidence of disoxic/anoxic conditions that has been highlighted in Section N-O by Tomimatsu et al. (2021) (Figs. 2 and 3). Alternatively, the negative values in the Δ^{199}Hg could be due to changes in the relative proportion of atmospheric vs terrigenous Hg. Understanding the significance of such features of the Δ^{199}Hg record of Section N-O will, however, require further investigation.

After the CPE (from ~12.5 m to the top of Section N-O), a Δ^{199}Hg decrease coincides with low values of Hg concentrations, Hg/TOC, Hg/Al_{EF}, Hg/Th_{EF}, Hg/Zn_{EF}, Hg/Ni_{EF}, Cu_{EF}/V_{EF} ratios (Figs. 2 and 3). This may suggest that the primary source of Hg was again dominantly terrestrial which may be consistent with the fading of the Wrangellia volcanism whose latest products are roughly dated to the early Tuvalian (e.g., Dal Corso et al., 2020). The explanation of the Δ^{199}Hg record after the CPE requires further study.

In summary, the data presented above show that multiple lines of evidence point to a period of intense activity of the Wrangellia LIP during the late Julian/early Tuvalian. Most notably, the Julian/Tuvalian transition is a particularly relevant time during the CPE. Approximately 33% of marine genera went extinct or severely declined in number and diversity at the Julian/Tuvalian boundary interval (e.g., Dal Corso et al., 2020). High-resolution biodiversity data show that ammonoids and conodonts underwent major turnover, and oxygen isotopes data from conodont apatite suggest that highest temperatures were reached (Fig. 1A; e.g., Hornung et al., 2007; Rigo et al., 2007; Dal Corso et al., 2020). In terrestrial settings, the Julian/Tuvalian transition is when the radiation and diversification of several plant groups occurred (Fig. 1A; Dal Corso et al., 2020). Increased amber content in sediments, interpreted as evidence for stressed conditions of terrestrial ecosystems, possibly due to increased occurrence of storms and wildfires, begins in the late Julian (Fig. 1A; e.g., Seyfullah et al., 2018). Recently, a Tethys-wide sea-level drop has been documented after the onset of NCIE 1, but prior to the NCIE 3 of the CPE (late Julian; Jin et al., 2022a). This sea-level fall was followed by the deposition of oolitic bodies interpreted as potential evidence of a chemical

calcification overshoot in marine environments possibly connected to ocean acidification (Jin et al., 2022a). Modeling carried out at the latest Permian extinction (Grasby et al., 2020) has shown that most intense pulses in volcanic activity of the Siberian Traps LIP would have emitted huge volumes of Hg able to induce heavy toxic shocks into marine and terrestrial environments. The fact that major transformation and evidence of biotic crises at the CPE coincide with what our data point to be a phase of particularly intense volcanic activity of the Wrangellia LIP are in agreement with this scenario and provide direct evidence of what have been suggested by models, potentially indicating that high intensity volcanism could be the main "killer" during mass extinction events.

6. Conclusions

In this work, Hg abundance and isotope data, along with other associated elements, are presented from a Carnian pelagic succession from the central Panthalassic Ocean encompassing the Carnian Pluvial Episode. Four synchronous peaks in Hg concentrations, Hg/TOC, Hg/Al_{EF}, Hg/Th_{EF}, Hg/Zn_{EF}, and Hg/Ni_{EF} ratios associated with near-zero $\Delta^{199}Hg$ values and increased Cu loading are observed, and provide evidence of multiple phases of Wrangellia LIP activity, along with Hg and Cu input, during the CPE.

The onset of Hg loading precedes the CPE onset in agreement with other evidence indicating that volcanic activity initiated prior to the CPE siliciclastic input. $\Delta^{199}Hg$ values at the Julian/Tuvalian boundary are suggestive of a particularly intense and prolonged phase in the volcanic activity of the Wrangellia LIP and are associated with excess Hg and Cu loading into the rocks. This suggests that this climax in Wrangellia volcanism produced an enhanced flux of Hg and other potentially toxic elements into the environment at the Julian/Tuvalian transition. Most notably this is when major climate changes and biological turnovers during the CPE occurred.

Our findings provide direct evidence in support of models that show LIPs are characterized by an irregular activity pattern with phases of particularly intense eruptions when huge amounts of toxic elements could be released into the atmosphere/ocean system, potentially becoming the major cause of biotic and environmental crises.

CRediT authorship contribution statement

X.J. conceived the idea and primarily wrote the manuscript with valuable input from M.F.; Y.T. participated in field works, reviewed and modified the text; R.S.Y. performed Hg isotope analysis, Hg concentration analysis, trace elements analysis, reviewed and modified the text; T.O participated in field works, reviewed and modified the text; M.F., S.E.G., Y.X.D., M.R. reviewed and modified the text. All authors contributed to the discussion and interpretation of the data.

Declaration of competing interest

The authors declare that they have no known competing financial interests or personal relationships that could have appeared to influence the work reported in this paper.

Data availability

Data will be made available on request.

Acknowledgements

We are grateful to the editor Prof. Andrew Jacobson and two anonymous reviewers for their constructive comments. We also thank Nereo Preto and Piero Gianolla for helpful discussions. This work was supported by the National Natural Science Foundation of China grants (42272128; 42293291). This is a contribution to the IGCP 739 (The Mesozoic-Palaeogene hyperthermal events).

Appendix A. Supplementary material

Supplementary material related to this article can be found online at https://doi.org/10.1016/j.epsl.2023.118075.

References

Algeo, T.J., Maynard, J.B., 2004. Trace-element behavior and redox facies in core shales of Upper Pennsylvanian Kansas-type cyclothems. Chem. Geol. 206, 289–318.
Ando, A., Kodama, K., Kojima, S., 2001. Low-latitude and Southern Hemisphere origin of Anisian (Triassic) bedded chert in the Inuyama area, Mino terrane, central Japan. J. Geophys. Res., Solid Earth 106, 1973–1986.
Baranyi, V., Rostási, Á., Raucsik, B., Kürschner, W.M., 2019. Palynology and weathering proxies reveal climatic fluctuations during the Carnian Pluvial Episode (CPE) (Late Triassic) from marine successions in the Transdanubian Range (western Hungary). Glob. Planet. Change 177, 157–172.
Bergquist, B.A., 2017. Mercury, volcanism, and mass extinctions. Proc. Natl. Acad. Sci. 114, 8675–8677.
Bergquist, B.A., Blum, J.D., 2007. Mass-dependent and -independent fractionation of Hg isotopes by photoreduction in aquatic systems. Science 318, 417–420.
Bernardi, M., Gianolla, P., Petti, F.M., Mietto, P., Benton, M.J., 2018. Dinosaur diversification linked with the Carnian Pluvial Episode. Nat. Commun. 9, 1499.
Blum, J.D., Bergquist, B.A., 2007. Reporting of variations in the natural isotopic composition of mercury. Anal. Bioanal. Chem. 388, 353–359.
Blum, J.D., Sherman, L.S., Johnson, M.W., 2014. Mercury isotopes in Earth and environmental sciences. Annu. Rev. Earth Planet. Sci. 42, 249–269.
Breda, A., Preto, N., Roghi, G., Furin, S., Meneguolo, R., Ragazzi, E., Fedele, P., Gianolla, P., 2009. The Carnian Pluvial Event in the Tofane area (Cortina d'Ampezzo, Dolomites, Italy). Geo Alp 6, 80–115.
Cho, T., Ikeda, M., Ohta, T., 2022. Increased terrigenous supply to the pelagic Panthalassa Superocean across the Carnian Pluvial Episode: a possible link with extensive aridification in the Pangean interior. Front. Earth Sci. 10, 897396.
Chu, D., Corso, J.D., Shu, W., Song, H., Wignall, P.B., Grasby, S.E., Schootbrugge, B.v.d., Zong, K., Wu, Y., Tong, J., 2021. Metal-induced stress in survivor plants following the end-Permian collapse of land ecosystems. Geology 49, 657–661.
Cossa, D., Mucci, A., Guédron, S., Coquery, M., Radakovitch, O., Escoube, R., Campillo, S., Heussner, S., 2021. Mercury accumulation in the sediment of the Western Mediterranean abyssal plain: a reliable archive of the late Holocene. Geochim. Cosmochim. Acta 309, 1–15.
Dal Corso, J., Bernardi, M., Sun, Y., Song, H., Seyfullah, L.J., Preto, N., Gianolla, P., Ruffell, A., Kustatscher, E., Roghi, G., 2020. Extinction and dawn of the modern world in the Carnian (Late Triassic). Sci. Adv. 6, eaba0099.
Dal Corso, J., Gianolla, P., Rigo, M., Franceschi, M., Roghi, G., Mietto, P., Manfrin, S., Raucsik, B., Budai, T., Jenkyns, H.C., 2018. Multiple negative carbon-isotope excursions during the Carnian Pluvial Episode (Late Triassic). Earth-Sci. Rev. 185, 732–750.
Deng, C., Sun, G., Rong, Y., Sun, R., Sun, D., Lehmann, B., Yin, R., 2021. Recycling of mercury from the atmosphere-ocean system into volcanic-arc–associated epithermal gold systems. Geology 49, 309–313.
Dolenec, T., Lojen, S., Ramovš, A., 2001. The Permian–Triassic boundary in Western Slovenia (Idrijca Valley section): magnetostratigraphy, stable isotopes, and elemental variations. Chem. Geol. 175, 175–190.
Furin, S., Preto, N., Rigo, M., Roghi, G., Gianolla, P., Crowley, J.L., Bowring, S.A., 2006. High-precision U-Pb zircon age from the Triassic of Italy: implications for the Triassic time scale and the Carnian origin of calcareous nannoplankton and dinosaurs. Geology 34, 1009–1012.
Gobeil, C., Macdonald, R.W., Smith, J.N., 1999. Mercury profiles in sediments of the Arctic Ocean basins. Environ. Sci. Technol. 33, 4194–4198.
Grasby, S.E., Sanei, H., Beauchamp, B., Chen, Z., 2013. Mercury deposition through the Permo–Triassic biotic crisis. Chem. Geol. 351, 209–216.
Grasby, S.E., Liu, X., Yin, R., Ernst, R.E., Chen, Z., 2020. Toxic mercury pulses into late Permian terrestrial and marine environments. Geology 48, 830–833.
Grasby, S.E., Shen, W., Yin, R., Gleason, J.D., Blum, J.D., Lepak, R.F., Hurley, J.P., Beauchamp, B., 2017. Isotopic signatures of mercury contamination in latest Permian oceans. Geology 45, 55–58.
Grasby, S.E., Them Ii, T.R., Chen, Z., Yin, R., Ardakani, O.H., 2019. Mercury as a proxy for volcanic emissions in the geologic record. Earth-Sci. Rev. 196, 102880.
Greene, A.R., Scoates, J.S., Weis, D., Katvala, E.C., Israel, S., Nixon, G.T., 2010. The architecture of oceanic plateaus revealed by the volcanic stratigraphy of the accreted Wrangellia oceanic plateau. Geosphere 6, 47–73.
Gusev, A.A., 2014. The fractal structure of the sequence of volcanic eruptions worldwide: order clustering of events and episodic discharge of material. J. Volcanol. Seismol. 8, 34–53.

Gworek, B., Bemowska-Kałabun, O., Kijeńska, M., Wrzosek-Jakubowska, J., 2016. Mercury in marine and oceanic waters—a review. Water Air Soil Pollut. 227, 1–19.
Hornung, T., Brandner, R., Krystyn, L., Joachimski, M.M., Keim, L., 2007. Multistratigraphic constraints on the NW Tethyan "Carnian Crisis". Glob. Triassic 41, 59–67.
Jin, X., Franceschi, M., Martini, R., Shi, Z.Q., Gianolla, P., Rigo, M., Wall, C.J., Schmitz, M.D., Lu, G., Du, Y.X., Huang, X.T., Preto, N., 2022a. Eustatic sea-level fall and global fluctuations in carbonate production during the Carnian Pluvial Episode. Earth Planet. Sci. Lett. 594, 117698.
Jin, X., Ogg, J.G., Lu, S., Shi, Z., Kemp, D.B., Hua, X., Onoue, T., Rigo, M., 2022b. Terrestrial record of carbon-isotope shifts across the Norian/Rhaetian boundary: a high-resolution study from northwestern Sichuan Basin, South China. Glob. Planet. Change 210, 103754.
Jin, X., Gianolla, P., Shi, Z., Franceschi, M., Caggiati, M., Du, Y., Preto, N., 2020. Synchronized changes in shallow water carbonate production during the Carnian Pluvial Episode (Late Triassic) throughout Tethys. Glob. Planet. Change 184, 103035.
Kongchum, M., Hudnall, W.H., Delaune, R., 2011. Relationship between sediment clay minerals and total mercury. J. Environ. Sci. Health, Part A 46, 534–539.
Liang, Q., Grégoire, D.C., 2000. Determination of trace elements in twenty six Chinese geochemistry reference materials by inductively coupled plasma-mass spectrometry. Geostand. Newsl. 24, 51–63.
Lu, J., Zhang, P., Dal Corso, J., Yang, M., Wignall, P.B., Greene, S.E., Shao, L., Lyu, D., Hilton, J., 2021. Volcanically driven lacustrine ecosystem changes during the Carnian Pluvial Episode (Late Triassic). Proc. Natl. Acad. Sci. 118, e2109895118.
Matsuda, T., Isozaki, Y., 1991. Well-documented travel history of Mesozoic pelagic chert in Japan: from remote ocean to subduction zone. Tectonics 10, 475–499.
Matsuoka, A., 1994. Triassic-Jurassic radiolarian-bearing sequences in the Mino Terrance, Central Japan. InterRad VII Field Excursion II (Mesozoic). Organ. Comm. InterRad 1994, 19–61.
Mazaheri-Johari, M., Gianolla, P., Mather, T.A., Frieling, J., Chu, D., Dal Corso, J., 2021. Mercury deposition in Western Tethys during the Carnian Pluvial Episode (Late Triassic). Sci. Rep. 11, 1–10.
Moore, C.R., Brooks, M.J., Goodyear, A.C., Ferguson, T.A., Perrotti, A.G., Mitra, S., Listecki, A.M., King, B.C., Mallinson, D.J., Lane, C.S., 2019. Sediment cores from White Pond, South Carolina, contain a platinum anomaly, pyrogenic carbon peak, and coprophilous spore decline at 12.8 ka. Sci. Rep. 9, 1–11.
Parrish, R.R., McNicoll, V., 1992. U-Pb age determinations from the southern Vancouver Island area, British Columbia. Radiogenic age and isotopic studies. Report 5, 91–92.
Rigo, M., Joachimski, M.M., 2010. Palaeoecology of Late Triassic conodonts: constraints from oxygen isotopes in biogenic apatite. Acta Palaeontol. Pol. 55, 471–478.
Rigo, M., Mazza, M., Karádi, V., Nicora, A., 2018. New Upper Triassic Conodont Biozonation of the Tethyan Realm, The Late Triassic World. Springer, pp. 189–235.
Rigo, M., Preto, N., Roghi, G., Tateo, F., Mietto, P., 2007. A rise in the Carbonate Compensation Depth of western Tethys in the Carnian (Late Triassic): deep-water evidence for the Carnian Pluvial Event. Palaeogeogr. Palaeoclimatol. Palaeoecol. 246, 188–205.
Rigo, M., Trotter, J.A., Preto, N., Williams, I.S., 2012. Oxygen isotopic evidence for Late Triassic monsoonal upwelling in the northwestern Tethys. Geology 40, 515–518.
Roghi, G., 2004. Palynological investigations in the Carnian of the Cave del Predil area (Julian Alps, NE Italy). Rev. Palaeobot. Palynol. 132, 1–35.
Roghi, G., Gianolla, P., Kustatscher, E., Schmidt, A.R., Seyfullah, L.J., 2022. An exceptionally preserved terrestrial record of LIP effects on plants in the Carnian (Upper Triassic) amber-bearing section of the dolomites, Italy. Front. Earth Sci. 10, 900586.
Rudnick, R.L., Gao, S., 2014. 4.1 - Composition of the continental crust. In: Holland, H.D., Turekian, K.K. (Eds.), Treatise on Geochemistry, second edition. Elsevier, Oxford, pp. 1–51.
Schoene, B., Eddy, M.P., Samperton, K.M., Keller, C.B., Keller, G., Adatte, T., Khadri, S.F., 2019. U-Pb constraints on pulsed eruption of the Deccan Traps across the end-Cretaceous mass extinction. Science 363, 862–866.
Scotese, C.R., 2014. Atlas of Middle & Late Permian and Triassic Paleogeographic Maps, maps 43 - 48 from Volume 3 of the PALEOMAP Atlas for ArcGIS (Jurassic and Triassic) and maps 49 – 52 from volume 4 of the PALEOMAP PaleoAtlas for ArcGIS (Late Paleozoic), Mollweide Projection, PALEOMAP Project, Evanston, IL.
Selin, N.E., 2009. Global biogeochemical cycling of mercury: a review. Annu. Rev. Environ. Resour. 34, 43–63.
Seyfullah, L.J., Roghi, G., Dal Corso, J., Schmidt, A.R., 2018. The Carnian Pluvial Episode and the first global appearance of amber. J. Geol. Soc. 175, 1012–1018.
Shen, J., Algeo, T.J., Planavsky, N.J., Yu, J., Feng, Q., Song, H., Song, H., Rowe, H., Zhou, L., Chen, J., 2019. Mercury enrichments provide evidence of Early Triassic volcanism following the end-Permian mass extinction. Earth-Sci. Rev. 195, 191–212.
Shen, J., Yin, R., Algeo, T.J., Svensen, H.H., Schoepfer, S.D., 2022a. Mercury evidence for combustion of organic-rich sediments during the end-Triassic crisis. Nat. Commun. 13, 1–8.
Shen, J., Algeo, T.J., Feng, Q., 2022b. Mercury isotope evidence for a non-volcanic origin of Hg spikes at the Ordovician-Silurian boundary, South China. Earth Planet. Sci. Lett. 594, 117705.
Simms, M.J., Ruffell, A.H., 1989. Synchroneity of climatic change and extinctions in the Late Triassic. Geology 17, 265.
Soua, M., 2014. Early Carnian anoxic event as recorded in the southern Tethyan margin, Tunisia: an overview. Int. Geol. Rev. 56, 1884–1905.
Stanley Jr, G.D., 2003. The evolution of modern corals and their early history. Earth-Sci. Rev. 60, 195–225.
Sugiyama, K., 1977. Triassic and Lower Jurassic radiolarian biostratigraphy in the siliceous claystone and bedded chert units of the southeastern Mino Terrane, Central Japan. Bull. Mizunami Fossil Mus. 24, 79–193.
Sun, Y.D., Wignall, P.B., Joachimski, M.M., Bond, D.P.G., Grasby, S.E., Lai, X.L., Wang, L.N., Zhang, Z.T., Sun, S., 2016. Climate warming, euxinia and carbon isotope perturbations during the Carnian (Triassic) Crisis in South China. Earth Planet. Sci. Lett. 444, 88–100.
Them, T.R., Jagoe, C.H., Caruthers, A.H., Gill, B.C., Grasby, S.E., Gröcke, D.R., Yin, R., Owens, J.D., 2019. Terrestrial sources as the primary delivery mechanism of mercury to the oceans across the Toarcian Oceanic Anoxic Event (Early Jurassic). Earth Planet. Sci. Lett. 507, 62–72.
Thibodeau, A.M., Bergquist, B.A., 2017. Do mercury isotopes record the signature of massive volcanism in marine sedimentary records? Geology 45, 95–96.
Tomimatsu, Y., Nozaki, T., Sato, H., Takaya, Y., Kimura, J.-I., Chang, Q., Naraoka, H., Rigo, M., Onoue, T., 2021. Marine osmium isotope record during the Carnian "pluvial episode" (Late Triassic) in the pelagic Panthalassa Ocean. Glob. Planet. Change 197, 103387.
Tomimatsu, Y., Onoue, T., Rigo, M., 2022. Conodont and radiolarian biostratigraphic age constraints on Carnian (Upper Triassic) chert-hosted stratiform manganese deposits from Panthalassa: formation of deep-sea mineral resources during the Carnian pluvial episode. Mar. Micropaleontol. 171, 102084.
Trotter, J.A., Williams, I.S., Nicora, A., Mazza, M., Rigo, M., 2015. Long-term cycles of Triassic climate change: a new $\delta^{18}O$ record from conodont apatite. Earth Planet. Sci. Lett. 415, 165–174.
Uno, K., Onoue, T., Hamada, K., Hamami, S., 2012. Palaeomagnetism of Middle Triassic red bedded cherts from southwest Japan: equatorial palaeolatitude of primary magnetization and widespread secondary magnetization. Geophys. J. Int. 189, 1383–1398.
Wakita, K., 1988. Origin of chaotically mixed rock bodies in the Early Jurassic to Early Cretaceous sedimentary complex of the Mino terrane, central Japan. Bull. Geol. Surv. Jpn. 39 (11), 675–757.
Wang, X., Cawood, P.A., Zhao, H., Zhao, L., Grasby, S.E., Chen, Z.-Q., Wignall, P.B., Lv, Z., Han, C., 2018. Mercury anomalies across the end Permian mass extinction in South China from shallow and deep water depositional environments. Earth Planet. Sci. Lett. 496, 159–167.
Yager, J.A., West, A.J., Thibodeau, A.M., Corsetti, F.A., Rigo, M., Berelson, W.M., Bottjer, D.J., Greene, S.E., Ibarra, Y., Jadoul, F., 2021. Mercury contents and isotope ratios from diverse depositional environments across the Triassic–Jurassic Boundary: towards a more robust mercury proxy for large igneous province magmatism. Earth-Sci. Rev. 223, 103775.
Yamashita, D., Kato, H., Onoue, T., Suzuki, N., 2018. Integrated Upper Triassic conodont and radiolarian biostratigraphies of the Panthalassa Ocean. Paleontol. Res. 22, 167–197.
Yin, R., Feng, X., Hurley, J.P., Krabbenhoft, D.P., Lepak, R.F., Hu, R., Zhang, Q., Li, Z., Bi, X., 2016. Mercury isotopes as proxies to identify sources and environmental impacts of mercury in sphalerites. Sci. Rep. 6, 1–8.
Zerkle, A.L., Yin, R., Chen, C., Li, X., Izon, G.J., Grasby, S.E., 2020. Anomalous fractionation of mercury isotopes in the Late Archean atmosphere. Nat. Commun. 11, 1–9.
Zhang, H., Zhang, F., Chen, J.-b., Erwin, D.H., Syverson, D.D., Ni, P., Rampino, M., Chi, Z., Cai, Y.-f., Xiang, L., 2021. Felsic volcanism as a factor driving the end-Permian mass extinction. Sci. Adv. 7, eabh1390.
Zhao, H., Grasby, S.E., Wang, X., Zhang, L., Liu, Y., Chen, Z.-Q., Hu, Z., Huang, Y., 2022. Mercury enrichments during the Carnian Pluvial Event (Late Triassic), South China. Geol. Soc. Am. Bull. 134, 2709–2720.